RSC Advances

ROYAL SOCIETY OF CHEMISTRY

www.rsc.org/advances

Journal Name

RSCPublishing

ARTICLE

Enhanced lithium storage capability of dual-phase $Li_4Ti_5O_{12}$-TiO_2/carbon nanofibers anode with interfacial pseudocapacitive effect

Jiangman Sun, DonghuaTeng, Yuan Liu, Cheng Chi, Yunhua Yu*, Jin-Le Lan and Xiaoping Yang

Cite this: DOI: 10.1039/x0xx00000x

Received 00th January 2012,
Accepted 00th January 2012

DOI: 10.1039/x0xx00000x

www.rsc.org/

Hydrothermal treatments of electrospun titanium dioxide/carbon nanofibers (TiO_2/CNFs) in LiOH solution were performed in a temperature range of 130-190 ºC, and then followed by a thermal treatment at 600 ºC in N_2 atmosphere. The changes in morphologies, microstructures and compositions as well as the electrochemical performances with hydrothermal temperatures were investigated for all samples. The morphological and compositional characterizations showed that the surfaces of CNFs-matrix were covered by numerous nanoparticles with size distributions of 25-100 nm. For the sample hydrothermally treated at 150 ºC (denoted as LC-150), these nanoparticles (~25 nm) were composed of well-crystalline spinel $Li_4Ti_5O_{12}$ and anatase TiO_2 with abundant phase interfaces and grain boundaries, which can induce the interfacial pseudocapacitive effect. Therefore, the as-prepared dual-phase structured $Li_4Ti_5O_{12}$-TiO_2/CNFs sample as a binder-free anode for lithium-ion batteries (LIBs) presented a greatly enhanced reversible capacity (203.8 mA h g^{-1} at 100 mA g^{-1} after 200 cycles) and a favored rate capability (114.3 mA h g^{-1} at 2000 mA g^{-1}) compared with the single-phase $Li_4Ti_5O_{12}$/CNFs sample.

1. Introduction

With growing concerns over a series of current international issues such as global warming and oil crisis, it is significant to develop new power sources for renewable energy systems. Lithium-ion batteries (LIBs) have been regarded as one of the most promising energy storage technologies for various portable electronics devices, electric vehicles (EVs) and plug-in hybrid electric vehicles (PHEVs) [1-3]. However, one of the crucial safety concerns has arisen because of the dendritic lithium growth on electrode surface because the operating voltage of commercial carbonaceous anode materials approaches almost 0 V vs. Li/Li^+ at the end of Li insertion [4, 5]. Spinel lithium titanium oxide ($Li_4Ti_5O_{12}$) exhibits excellent reversibility and good safety due to the unique near-zero structural changes during repeated Li-ion insertion/extraction processes and extremely flat discharge plateau at about 1.5 V (vs. Li/Li^+) [6-8]. Thus, it is considered as a promising substitute for carbonaceous anodes. However, its intrinsic low reversible capacity (theoretical capacity: 175 mA h g^{-1}) and extremely low electronic conductivity (10^{-13} S m^{-1}) at room temperature lead to poor rate capability, failing to satisfy the requirements of LIBs at high current densities [9-11].

Many strategies have been developed to overcome the obstacles of $Li_4Ti_5O_{12}$. Reducing the particle size of $Li_4Ti_5O_{12}$ to nanoscale range has been proposed as an effectual method in previous work [10-12]. In comparison with bulk $Li_4Ti_5O_{12}$, nanostructured $Li_4Ti_5O_{12}$ anodes exhibit enhanced electrochemical performance due to shorter Li^+ diffusion paths and larger electrochemical interfaces [11-15]. Hydrothermal process has been proved as a useful method to prepare nanostructured $Li_4Ti_5O_{12}$ anodes with excellent electrochemical properties [11, 16]. Recently, Gao' group reported a dual-phase $Li_4Ti_5O_{12}$-TiO_2 anode for LIBs from hydrothermal process with thiourea [11], which delivered improved electrochemical performance over individual phase $Li_4Ti_5O_{12}$ and anatase TiO_2 due to the interfacial pseudocapacitive effect induced by abundant phase interfaces between spinel $Li_4Ti_5O_{12}$ and anatase TiO_2 as well as the faster Li ion insertion/extraction and higher theoretical capacity of nano-sized anatase TiO_2 (336 mAh g^{-1}) [10, 17-22]. However, the reversible capability of the dual-phase $Li_4Ti_5O_{12}$-TiO_2 anode is still limited by its low electronic conductivity. Usually, the approach to enhancing the electronic conductivity of electrodes is incorporating them with conductive carbonaceous materials such as graphite, carbon nanotubes, and especially electrospun carbon nanofibers (CNFs), which can render continuous e^- transportation pathways [23-25]. Nevertheless, to the best of our knowledge, there have been few reports on the effective modification of the $Li_4Ti_5O_{12}$ anodes by using the above-mentioned approaches.

Herein, we report on a nano-architectured dual-phase $Li_4Ti_5O_{12}$-TiO_2/CNFs film electrode fabricated by LiOH hydrothermal reaction of electrospun TiO_2/CNFs followed by a calcination treatment. The influences of hydrothermal temperatures on compositions, morphologies and electrochemical performances were discussed carefully. Moreover, the role of interfacial pseudocapacitive effect

induced by abundant phase interfaces between well-crystalline spinel $Li_4Ti_5O_{12}$ and anatase TiO_2 phases was interpreted in detail.

2. Experimental

2.1 Preparation

Customarily, anatase-TiO_2/CNFs and CNFs were synthesized according to our previous work [26]. As-prepared anatase-TiO_2/CNFs was put into a Teflon-lined autoclave (100 ml) with 40 ml LiOH solution (2 M) and then heat treated at 130, 150, 170 and 190 ºC for 24 h, respectively. After cooling down to room temperature, the resultant nanofibers were washed carefully with deionized water and ethanol followed by vacuum drying at 80 ºC for 12 h and finally calcined in nitrogen at 600 ºC for 4 h. According to different hydrothermal temperatures (130, 150, 170 and 190 ºC), the corresponding products were denoted as LC -130, LC -150, LC -170 and LC-190, respectively. For comparison, nano-$Li_4Ti_5O_{12}$ particles were also prepared by hydrothermal method according to previous paper [27] and calcined at 600 ºC for 4 h.

2.2Structural characterizations

Morphologies and compositions of the samples were evaluated using a field emission scanning electron microscope (FE-SEM, Supra55, CarlZeiss) and energy dispersive X-ray (EDX) spectroscopy attached to SEM. The average diameters of CNFs and nanoparticles interspersed on the CNFs were calculated based on the FESEM images using Image J software analyzer. Thermo gravimetric analysis (TGA) was carried out with a TGA instrument (TA-Q 50, America) at a heating rate of 10 ºC min^{-1} from 25 to 800 ºC in air. Transmission scanning electron (TEM, Tecnai $G^2$20, FEI) and high-resolution transmission electron microscope (HR-TEM, JEM-3010, JEOL) investigations were performed to further characterize the interior structure of samples. The crystal structures were examined by X-ray diffraction (XRD, Brucker NEW D8 Advance, Germany) with Ni-filtered Cu Kα radiation at 40 kV and 40 mA (λ = 0.154 nm). X-ray photoelectron spectroscopy (XPS, EscaLab250, and Thermo Fisher Scientific) experiments were carried out to analyze the chemical valence state of elements using monochromatic aluminum Kα X-ray radiation as the excitation source.

2.3 Electrochemical characterizations

Electrochemical properties were evaluated using 2025 coin cells assembled in a high-pure argon-filled glove box with lithium foil as the counter and reference electrodes according to our previous study [26, 28]. As-prepared samples and TiO_2/CNFs were directly employed as working electrodes without any additional conductive agent or binder. For comparison, mechanical $Li_4Ti_5O_{12}$-TiO_2-CNFs mixture electrode was prepared by mixing $Li_4Ti_5O_{12}$ nanoparticles, anatase TiO_2 (Aldrich) and CNFs in a weight ratio of 6.4: 1.6: 2. CNFs anode was prepared as a reference electrode mixed with Super-P-Li and PVDF in a weight ratio of 8:1:1. A solution of 1M $LiPF_6$ in ethylene carbonate/dimethyl carbonate (EC: DMC, 1:1 by volume) and Celgard 2300 membrane were chosen as the electrolyte and the separator, respectively.

Assembled cells were charged and discharged on a battery instrument (LAND-CT2001A) at a constant current density of 100 mA g^{-1} or at different current densities of 100, 200, 500, 1000 and 2000 mA g^{-1}. Specific capacities were calculated based upon the mass of active substances ($Li_4Ti_5O_{12}$ and TiO_2). Cyclic voltammetry (CV) experiments were performed using a work station (Auto lab PGSTAT 302 N Metrohm) at a scan rate of 0.2 mV s^{-1} or at different scan rates of 0.2, 0.5, 1, 2 and 5 mV s^{-1}, respectively. Electrochemical impedance spectrum (EIS) measurements were conducted on the same workstation after 200 cycles with amplitude of 10 mV and a frequency range from 10 kHz to 0.1 Hz. Potential voltage range varied from 1 to 3 V (vs. Li/Li^+) during all the electrochemical measurements at ambient temperature.

3. Results and discussion

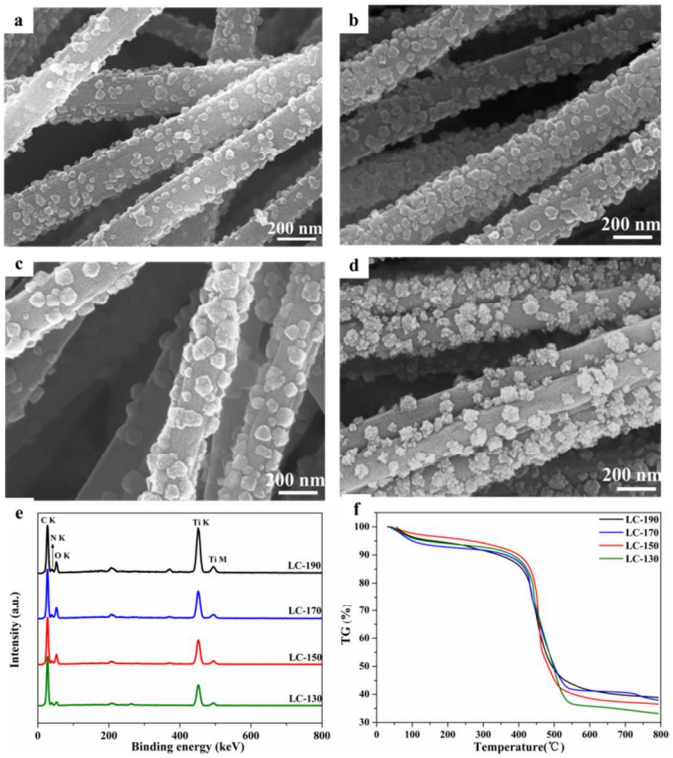

Fig. 1 SEM images of (a): LC-130, (b): LC-150, (c): LC-170 and (d): LC-190. (e) EDX patterns and (f) TGA curves of all four samples.

Morphological characterizations and compositional evaluations of samples obtained at different hydrothermal temperatures (LC-130, LC-150, LC-170, and LC-190) are displayed in Fig. 1. FE-SEM images (Fig. 1a~d) reveal clearly that all samples exhibit continuous fibrous morphologies with relatively uniform diameters ranging from 200 to 300 nm. The CNFs with partial alignment are interspersed with numerous nanoparticles, which are confirmed as spinel $Li_4Ti_5O_{12}$ and/or anataseTiO_2 crystalline by EDX spectrum (Fig.1e), SAED pattern (inset in Fig.2c and 2d) and later XRD analysis (Fig. 3). The surface morphologies and formation of $Li_4Ti_5O_{12}$ can be attributed to the migration-corrosion-dissolution-nucleation growth mechanism. With high pressure and elevated temperature during hydrothermal environment, LiOH and H_2O molecules penetrate into the stabilized CNFs along nanopores to

generate erosion reaction with TiO_2 nanoparticles [29-31], which are dispersed uniformly in the support of CNFs (see the Supporting Information, Fig. S1). Therefore, TiO_2 gradually vacate from CNFs to cause micropores (see the Supporting Information Fig. S2) [30], and moderately nucleate with LiOH to hydrated $Li_4Ti_5O_{12}$ nanoparticles. With the subsequent calcination treatment, the lithium titanate compound can be dehydrated and thus the well-crystallized $Li_4Ti_5O_{12}$ with advantage of maintaining the elegant fibrous morphology and network structure of CNFs are formed. It is noted that the particle sizes tend to grow larger with the increase of hydrothermal temperature, as shown in Fig. S3. Compared with the average particle sizes of other three samples (20 nm, 25 nm and 60 nm for the LC-130, LC-150 and LC-170, respectively), the nanoparticles of LC-190 present diameters of about 100 nm and even show a relatively wide range in particle size distribution with significant particle aggregation. Therefore, the LC-150 and LC-170 are expected to deliver excellent electrochemical performances. Calculated from semi-quantitative EDX spectra and quantitative TGA curves (Fig.1e and 1f), all the four samples show similar compositions, which are composed of about 37 wt. % active substances and 63 wt. % CNFs.

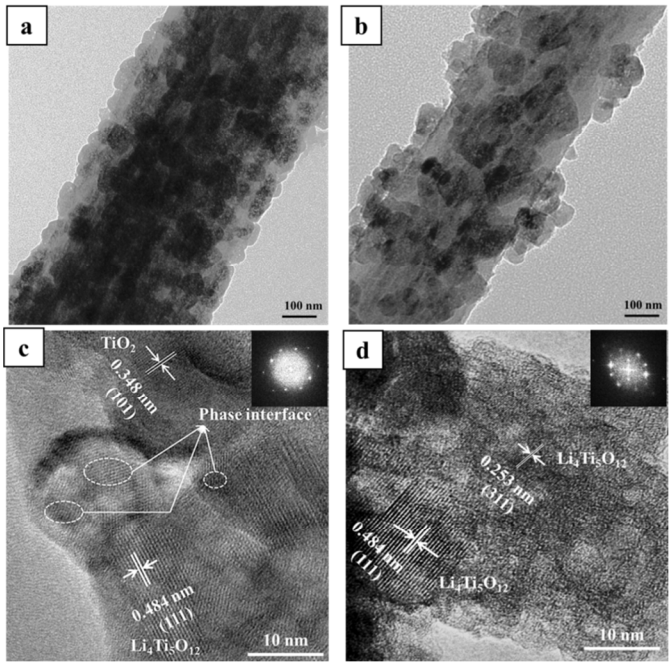

Fig. 2 (a, b) TEM and (c, d) HRTEM images with corresponding SAED patterns (inset) of a, c (LC-150) and b, d (LC-170).

To further examine the architectures of LC-150 and LC-170 samples，TEM and HRTEM characterizations were investigated (Fig. 2). Detailed information of the nanoparticles interspersed on CNFs can be illustrated by TEM images (Fig. 2a and 2b). The surfaces of CNFs are covered with numerous nanoparticles. While some spots of nanocrystals exist in the interior of CNFs (dark region in Fig. S2). What's more, the nanoparticle sizes of the LC-170 are larger than those of the LC-150, which is consistent with the SEM results (Fig. 1 and Fig. S3). Fig. 2c and 2d show distinctly that both the LC-150 and the LC-170 samples have lattice fringes of 0.484 and 0.253 nm, corresponding to the (111) and (311) interplanar spacings of spinel phase $Li_4Ti_5O_{12}$, respectively. However, the LC-150 has other fringe spacing of 0.348 nm belonging to the (101) plane of anatase TiO_2 [10, 11]. The crystal structures of the LC-150 and the LC-170 can also be testified by their SAED patterns (inset in Fig.2c and 2d). The corresponding SAED patterns of the LC-150 (inset in Fig. 2c) show several diffraction rings, which are assigned to the spinel $Li_4Ti_5O_{12}$ and anatase TiO_2 polycrystals [32]. Most importantly, the LC-150 demonstrates conspicuous grain boundaries and abundant phase interfaces (Fig. 2c), which are particularly favorable for the pseudocapacitive process to enhance its lithium storage capability [8, 11].

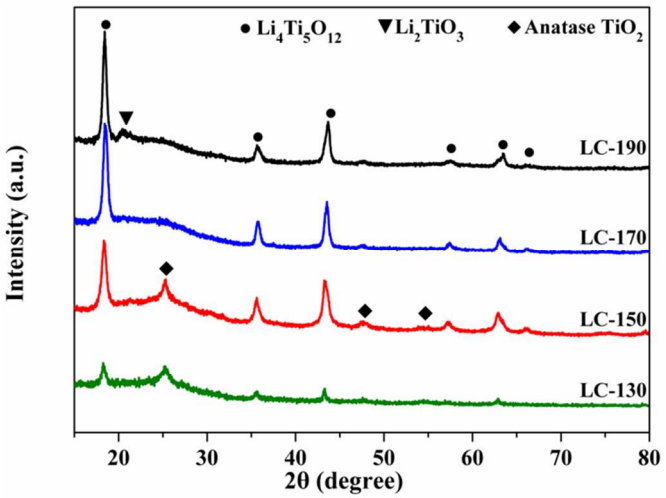

Fig. 3 XRD patterns of LC-130, LC-150, LC-170 and LC-190.

XRD patterns in Fig. 3 show that all samples exhibit broad peaks between 15º and 25º, indicating the formation of amorphous carbon (JCPDS Card No. 13-0148) [26]，which was further confirmed using Raman characterization (see the Supporting Information, Fig. S4). All the four samples showed well-known D-band (disorder-induced phonon mode at 1360 cm^{-1}) and G-band (E_{2g2} graphitic mode at 1588 cm^{-1}). However, the convolutional intensity ratios (I_D/I_G) of D-band to G-band for all the samples were around 1.200. So the carbon calcined at low temperature of 600 ºC showed low degree of graphitization. Moreover, all samples exhibit significant peaks at 18.4°, 35.6°, 43.3° , and 62.8° respectively, indexed to (111), (311), (400), and (440) reflections of spinel $Li_4Ti_5O_{12}$ structure (JCPDS Card No.49-0207). This confirms that a face-centered cubic spinel $Li_4Ti_5O_{12}$ with the *Fd3m* space group can be successfully synthesized through calcination treatment at 600 ºC in nitrogen. Meanwhile, additional peaks at 25.4° and 48.1° corresponding to (101) and (200) planes of anatase TiO_2 (JCPDS Card No.89-4921) are also observed in the XRD pattern of LC-130 and LC-150. But the LC-150 shows stronger diffraction peaks of $Li_4Ti_5O_{12}$ and slightly enhanced XRD peaks of anatase TiO_2. However, the LC-170 exhibits only a pure phase $Li_4Ti_5O_{12}$ with improved crystallinity. Furthermore, with the increase of hydrothermal temperature to 190 ºC, besides the main spinel $Li_4Ti_5O_{12}$ phase, a trace amount of impure phase, which can be well identified as Li_2TiO_3, are also observed in the diffraction peaks. XRD patterns of the four samples show clearly the transformation from anatase TiO_2 to spinel $Li_4Ti_5O_{12}$ with the increase of hydrothermal temperature. This suggests that elevated hydrotermal temperature assists pristine $Li_4Ti_5O_{12}$ phase to crystallize, agreeing well with the previous literature [10]. Moreover, the higher the hydrothermal temperature is, the narrower peak width at half height of XRD patterns becomes. That is to say, the average crystal sizes of nanoparticles begin to grow larger as the hydrothermal temperature increases, consistent with the results of SEM images (Fig. 2 and Fig. S2).

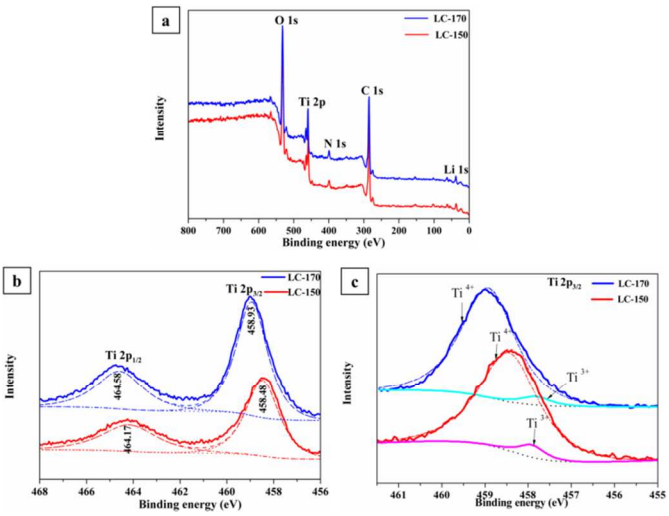

Fig.4 (a) XPS survey spectra and (b, c) XPS high resolution spectra of Ti_{2p} region of LC-150 and LC-170.

XPS characterizations were carried out to further investigate the surface chemical compositions and elemental states of samples. Fig. 4a depicts the XPS survey spectra of LC-150 and LC-170. Conspicuous O_{1s}, Ti_{2p}, N_{1s}, C_{1s} and Li_{1s} peaks are observed, indicating the presence of these five elements. According to the atomic percentage evaluated by XPS, the LC-150 is composed of 31.1 wt. % $Li_4Ti_5O_{12}$, 7.2 wt. % TiO_2 and 61.7 wt. % CNFs, while the LC-170 is composed of 38 wt. % $Li_4Ti_5O_{12}$ and 62 wt. % CNFs. So the CNFs content takes account of about 62 wt. % in both samples, which agrees well with the results of EDX and TGA (Fig.1e and 1f). Fig. 4b shows representative Ti_{2p} XPS spectra of both samples. Obviously, the Ti_{2p} spectrum for the LC-170 comprises two symmetrical peaks with bonding energies of 464.58 and 458.93 eV, attributable to $Ti_{2p1/2}$ and $Ti_{2p3/2}$, respectively, which are related to the Ti^{4+}. The LC-150 also presents similar $Ti_{2p1/2}$ and $Ti_{2p3/2}$ characteristic peaks, but the bonding energy values migrate to 464.16 and 458.48 eV, respectively. These micronic differences are probably ascribed to the increased oxygen vacancies in dual-phase $Li_4Ti_5O_{12}$-TiO_2 than those in pure $Li_4Ti_5O_{12}$ phase. The incremental oxygen vacancies can decrease electron cloud density surrounding the titanium core, so the electronic screening effect in the nanoparticles would be strengthened, causing the slightly decreased bonding energy values of the $Ti_{2p1/2}$ and $Ti_{2p3/2}$ signals. Such incremental oxygen vacancies are favorable to helping Li^+ insertion and movement of electrons [33-37], which is beneficial to improving electrochemical performance of the $Li_4Ti_5O_{12}$-TiO_2/CNFs electrode. In Fig. 4c, a more detailed analysis of $Ti_{2p3/2}$ reveals two peaks corresponding to Ti^{4+} and Ti^{3+}, respectively. The ratio of the [Ti^{3+}] / [Ti^{4+}] peak area increased from 0.04 (LC-170) to 0.06 (LC-150). The increase in Ti^{3+} content can contribute to increased electronic conductivity [38], which is expected to enhance the electrochemical performance of the active material.

The cyclic performances of LC-130, LC-150, LC-170 and LC-190 anodes at a current density of 100 mA g^{-1} in the potential range of 1-3 V (vs. Li/Li^+) are displayed in Fig. 5a. For comparison, mechanical $Li_4Ti_5O_{12}$-TiO_2-CNFs mixture and individual pure CNFs anodes were also tested. It is notable that the CNFs anode delivers a negligible discharge capacity of 13.3 mA h g^{-1} in the test voltage range. On the contrary, all other samples show high specific capacities in the range of 80-200 mA h g^{-1}. Among these five electrodes, the LC-130 and LC-190 deliver relatively lower specific capacities due to either poor crystallinity or particle aggregation, respectively. However, after 200 cycles, the LC-150 and the LC-170 anodes still present high discharge capacities of 203.8 and 154.6 mAh g^{-1}, respectively. Notably, the LC-150 anode shows superior reversible capacity than both the LC-170 and the mechanical $Li_4Ti_5O_{12}$-TiO_2-CNFs mixture (170.5 mA h g^{-1}) anodes. The enhanced cyclic performance of the LC-150 can be ascribed to the nano-sized $Li_4Ti_5O_{12}$ with shorter Li^+ diffusion paths and larger electrochemical interfaces. Meanwhile, we believe that the higher theoretical capacity of nano-sized anatase TiO_2, together with the interlaced CNFs matrix, contributes to the superior reversible capacity of the LC-150. The synergistic effects of fibrous carbon matrix and nano-composite structure established on the nanoweb architecture can guarantee electrolyte infiltrate intimately with active substances to expedite charge-transfer reaction. In particular, the abundant phase interfaces between $Li_4Ti_5O_{12}$ and TiO_2 in the LC-150 can induce faradic pseudocapacitive effect to provide extra locations to store lithium.

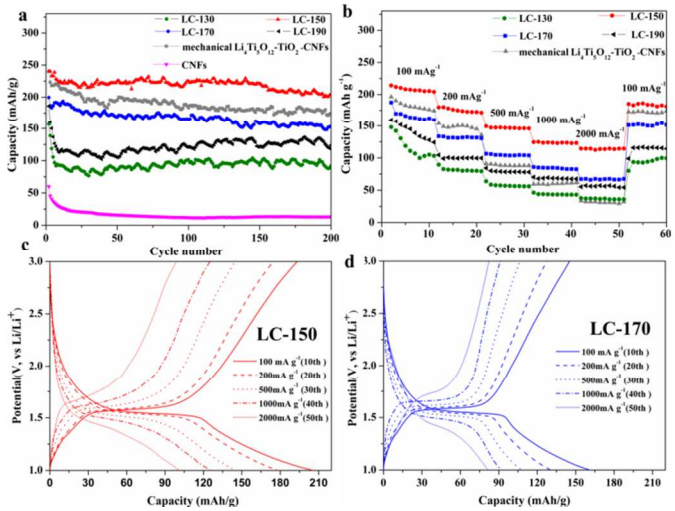

Fig. 5 (a) Cycling performance and (b) rate capabilities of LC-130, LC-150, LC-170 and LC-190; Charge-discharge profiles of c: LC-150 and d: LC-170.

Fig. 5b compares the rate performances of LC-130, LC-150, LC-170, LC-190 and mechanical $Li_4Ti_5O_{12}$-TiO_2-CNFs mixture anodes tested at various rates increased stepwise from 100 to 2000 mA g^{-1} in succession and finally back to 100 mA g^{-1}. With the increase of current densities, the rate capacities of all samples present a tendency to decrease progressively. Particularly, the specific reversible capacity of the mechanical $Li_4Ti_5O_{12}$-TiO_2-CNFs mixture declines most sharply, as shown in Fig. 5b. Nevertheless, the reversible capacity of LC-150 electrode drops most slowly than the other samples at the same rate. Even at the highest rate of 2000 mA g^{-1}, the LC-150 still remains a high capacity of 114.3 mA h g^{-1},which is much higher than the other four anodes (33.6, 37.8, 92.5 and 56.3 mA h g^{-1} for the mechanical $Li_4Ti_5O_{12}$-TiO_2-CNFs mixture, LC-130, LC-170, LC-190, respectively) and those reported in previous literature [10-15]. More importantly, when the current density is returned to initial value of 100 mA g^{-1} after a total period of 50 cycles, the discharge capacity of 185.1 mA h g^{-1} (86.4% of initial discharge capacity) is still available for the LC-150 with negligible losses for the next 10 cycles.

Fig. 5c and 5d show the charge/discharge curves of LC-150 and LC-170 anodes at different current densities in the voltage range of 1-3 V. Both anodes exhibit a pair of flat potential plateau around 1.55 V (vs. Li/Li^+) at 100 mA g^{-1}, associating to the dual-phase equilibrium between $Li_4Ti_5O_{12}$ and $Li_7Ti_5O_{12}$ [36]. Even at the high current density of 2000 mA g^{-1}, the LC-150 still maintains a flat potential plateau, indicating good reaction kinetics. However, with the increase of current densities, the LC-150 anode displays a relatively long platform. This identifies that the nano-sized TiO_2 with high reversible capacity and well-crystalline nanoparticles in LC-150 are favorable to enhancing the lithium storage capability of activated electrode [11, 24]. What's more, the LC-150 shows a flatter voltage plateaus than the LC-170. This is probably attributed to the faradaic pseudocapacitive effect induced by abundant interfaces of dual-phase LC-150.

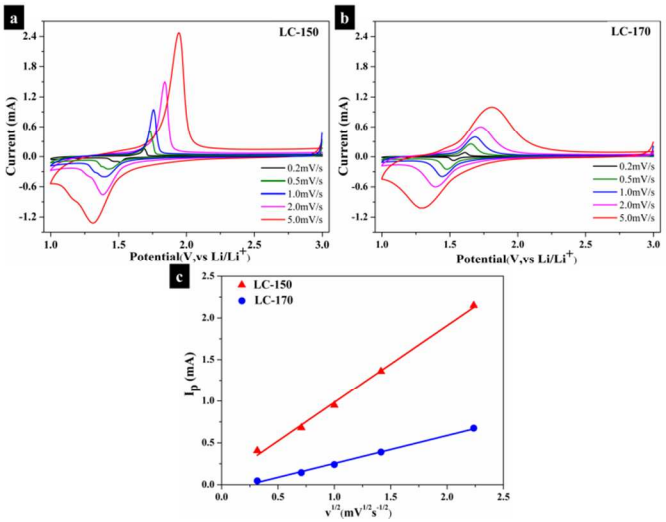

Fig. 6 Cyclic voltammograms with the relationships between the peak current and the scan rate in the anodic process ((c)) of (a): LC-150 and (b): LC-170 after 200 cycles at different scan rates of 0.2, 0.5, 1, 2 and 5 mV s^{-1}, respectively.

To interpret the superior electrochemical performance of the $Li_4Ti_5O_{12}$-TiO_2/CNFs anode, cyclic voltammogram (CV) measurements were performed on the as-prepared LC-150 and LC-170 anodes in the potential range of 1-3 V (Fig. 6). As presented in Fig. 6a and 6b,both the LC-150 and the LC-170 electrodes feature a pair of sharp potential peaks at around 1.5 V (vs. Li/Li^+) at 0.2 mV s^{-1}, agreeing well with the reported lithium ion insertion into/extraction out of the $Li_4Ti_5O_{12}$ [39]. In order to indicate the electrochemical kinetic diffusion-limited process of the reaction at around 1.5V (vs. Li/Li^+), a liner correlation between corresponding peak current and the square roots of scan rates was established (Fig. 6c) according to the Randles-Sevcik equation [12]:

$$I_p = 2.687*10^5\, An^{3/2}C_{Li}D_{Li}^{1/2}v^{1/2}\ (25℃) \quad (1)$$

The peak current is in the direct proportion to the square root of the scan rate for both LC-150 and LC-170 anodes (Fig. 6c). However, the oblique diagonal representing the LC-150 anode (red line) displays a much sharper slop, which suggests that lithium diffusion is easier and faster. Moreover, other potential peaks at 1.46, 1.34, 1.29, 1.26 and 1.16 V in the cathode process of the LC-150 appear more and more visible with the increase of the scan rate in Fig. 6a, while such peaks couldn't be observed in the cathode process of LC-170. Similar side peaks, which could induce pseudocapacitive effect, were also reported in previous literature [11, 24]. This further confirms the faradaic pseudocapacitive effect owning to the particular structure of dual-phase interphases, which is favorable to enhancing the electrochemical performance of $Li_4Ti_5O_{12}$-TiO_2/CNFs (LC-150). However, another pair of redox peaks of 1.71 and 2.10V (vs. Li/Li^+) due to the lithium ion reaction with anatase TiO_2, is not detected in the LC-150 electrode (Fig. 6a). The reason for disappearance of such pair of peaks in the CV curves of anatase TiO_2/CNFs electrode (Fig. S5), is probably ascribed to the unique structure of LC-150. During the migration-corrosion-dissolution-nucleation growth process, well-crystallized $Li_4Ti_5O_{12}$ nanoparticles interperse on the surface of nanofibers, accompanying the trace amount of nano-sized anatase TiO_2 dispersed in the interior of CNFs, so CV measurement could hardly detect the redox peaks of the TiO_2.

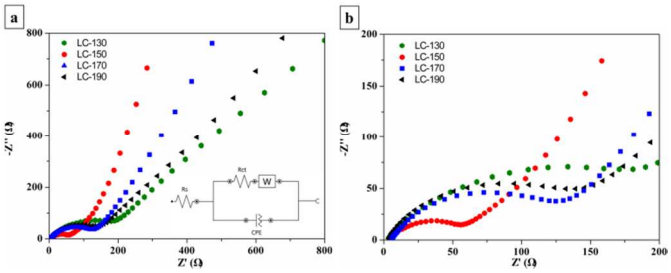

Fig. 7 Nyquist plots of LC-130, LC-150, LC-170 and LC-190.

Electrochemical impedance spectroscopy (EIS) tests were conducted in the frequency range from 0.01 to 100,000 Hz. Fig. 7 depicts the Nyquist plots of the LC-130, LC-150, LC-170 and LC-190 after 200 galvanostatic cycles at 100 mA g^{-1} with a corresponding equivalent circuit model. Typically, both the Nyquist plots consist of a depressed semicircle in the high-middle frequency regions and a slopping straight line in the low frequency region. The diameter of the semicircle is reflective of surface charge transfer resistance (R_{ct}), related to the interfacial electrochemical reaction activity. R_{ct} value (43.1Ω) of the LC-150 is much smaller than those of the LC-130 (151Ω), LC-170 (133 Ω) and LC-190 (200 Ω), corresponding to the exchange current densities i_0 calculated based on the following equation [12]:

$$i_0 = RT/nFR_{ct}A \quad (2)$$

Obviously, compared with the LC-170 anode, the LC-150 anode gives the easier and faster charge due to the abundant dual-phase interfaces and grain boundaries between $Li_4Ti_5O_{12}$and TiO_2 phases in LC-150 anode.

Benefiting from the unique structural and compositional merits, the LC-150 electrode exhibits exceptional electrochemical performance. First, the nanoparticles-micropores-nanofibers structure offers numerous interfaces, which can provide sufficient electrolyte-electrode contact area to expedite Li^+ insertion/extraction processes. Second, multi-component of well-crystallized $Li_4Ti_5O_{12}$ and TiO_2 nanoparticles interspersed uniformly on the CNFs matrix without aggregation plays a significant role in improving the specific reversible capacity and rate performance. Nano-sized anatase TiO_2 with higher theoretical capacity also contributes partial capacity to

the dual-phase $Li_4Ti_5O_{12}$-TiO_2/CNFs anode. Incremental oxygen vacancies and the increase in Ti^{3+} content are favorable to helping Li^+ insertion and movement of electrons as well. Furthermore, the interpenetrating network of CNFs forms a continuous electronic transportation path to reduce polarization resistance while offering high mechanical flexibility and structural integrity. Moreover, the abundant interfaces and grain boundaries provide more lithium storage sites, causing the enhancement of reversible capacity, especially for the improvement of rate capability. Meanwhile, the charge transfer impedance is decreased validly by the faradic pseudocapacitive effect, further beneficial to improving rate capability. Therefore, the dual-phase $Li_4Ti_5O_{12}$-TiO_2/CNFs anode (LC-150) exhibits superior rate capacity and stability.

Conclusions

To sum up, a dual-phase $Li_4Ti_5O_{12}$-TiO_2/CNFs nanocomposite with abundant phase interfaces and grain boundaries can be synthesized successfully by a hydrothermal reaction of electrospun anatase TiO_2/CNFs in LiOH solution and a subsequent calcination treatment. As-prepared $Li_4Ti_5O_{12}$-TiO_2/CNFs sample was evaluated by electrochemical measurements as a binder-free anode for LIBs, demonstrating better electrochemical performance over single-phase $Li_4Ti_5O_{12}$/CNFs and mechanical $Li_4Ti_5O_{12}$-TiO_2-CNFs mixture. The $Li_4Ti_5O_{12}$-TiO_2/CNFs anode delivers a favorable discharge capacity of 203.8 mA h g^{-1} after 200th cycle at 100 mA g^{-1} and still shows a relatively high discharge capacity of 114.3mA h g^{-1} at 2000 mA g^{-1}.The superior cycling performance and rate capability are mainly attributed to the interfacial pseudocapacitive effect combined with the advantages of conductive fibrous CNFs and high reversible capacity of well-crystallized $Li_4Ti_5O_{12}$ and TiO_2. Therefore, the dual-phase $Li_4Ti_5O_{12}$-TiO_2/CNFs nanocomposite holds great promise as a candidate anode for high-power LIBs.

Acknowledgements

This work was financially supported by National Natural Science Foundation of China (No. 51072013, 51272021 and 51142004) and Natural Science Foundation of Jiangsu Province (No. BK20131147).

Notes and references

State Key Laboratory of Organic-Inorganic Composites, Beijing University of Chemical Technology, Beijing 100029, China
* Corresponding author. Tel. /Fax: +8610-6442-7698/2084

E-mail address: yuyh@mail.buct.edu.cn

† Footnotes should appear here. These might include comments relevant to but not central to the matter under discussion, limited experimental and spectral data, and crystallographic data.
Electronic Supplementary Information (ESI) available: [details of any supplementary information available should be included here]. See DOI: 10.1039/b000000x/

1 M. Armand, J.-M.Tarascon, Nature, 2008, **451**, 652.
2 A.S. Arico, P. Bruse, B. Scrosati, J.-M. Tarascon, W. van Schalkwijk, Nat. Mater., 2005, **4**, 366.
3 K. Amine, I. Belharouak, Z.H. Chen, T. Tran, H. Yumoto, N. Ota, S.T. Myung, Y.K. Sun, Adv. Mater., 2010, **22**, 3052.
4 S. Flandrois, B. Simon, Carbon, 1999, **37**, 165.
5 H. Fujimoto, A. Mabuchi, K. Tokumitsu, N. Chinnasamy, T. Kasuh, J. Power Sources, 2011, **196**, 1365.
6 E.M. Sorensen, S.J. Barry, H.-K. Jung, J.M. Rondinelli, J.T. Vaughey, K.R. Poeppelmeier, Chem. Mater., 2005, **18**, 482.
7 L.F. Shen, C.Z. Yuan, H.J. Luo, X.G. Zhang, K. Xu, F. Zhang, J. Mater. Chem., 2011, **21**, 761.
8 S.H. Ju, Y.C. Kang, J. Power Sources, 2010, **195**, 4327.
9 L. Kavana, R. Bacsab, M. Tunckolb, P. Serpb, S.M. Zakeeruddinc, F.L. Formalc, M. Zukalovaa and M. Graetzelc, J. Power Sources, 2010, **195**, 5360.
10 G.Y. Liu, H.Y. Wang, G.Q. Liu, Z.Z. Yang, B. Jin, Q.C. Jiang, Electrochim Acta, 2013, **87**, 218.
11 X. Li, C. Lai, C.W. Xiao, X.P. Gao,Electrochim Acta, 2011, **56**, 9152.
12 J.Z. Chen, L. Yang, S.H. Fang, S. Hirano, K. Tachibana, J. Power Sources, 2012, **200**, 59.
13 A. Nugroho, S.J. Kim, W. Chang, K.Y. Chung, J. Kim, J. Power Sources, 2013, **244**, 164.
14 Y. Wang, H. Liu, K. Wang, H. Eiji, Y. Wang, H. Zhou, J. Mater. Chem., 2009, **19**, 6789.
15 Y. Wu, M.V. Reddy, B.V.R. Chowdari, S. Ramakrishna, Electrochim Acta,2012, **67**, 33.
16 J.R. Li, Z.L. Tang, Z.T. Zhang, Electrochem. Commun., 2005, **7**, 894.
17 S. Huang, Z. Wen, J. Zang, X. Yang, Electrochim Acta, 2007, **52**, 3704.
18 R. Cai, X. Yu, X. Liu, Z. Shao, J. Power Sources, 2010, **195**, 8244.
19 M.M. Rahman, J.Z. Wang, M.F. Hassan, S. Chou, D. Wexler, H.K. Liu, J. Power Sources, 2010, **195**, 4297.
20 B. Zhao, S. Jiang, C. Su, R. Cai, R. Ran, M.O. Tade, Z.P. Shao, J. Mater. Chem., 2013, **A1**,12310.
21 C. Lai, Y.Y. Dou, X. Li, J. Power Sources, 2010, **195**, 3676.
22 L. Kavan, M. Kalbac, M. Zukalova, I. Exnar, V. Lorenzen, R. Nesper, M. Graetzel, Chem. Mater., 2004, **16,** 477.
23 H.G. Jung, J. Kim, B. Scrosati, Y.K. Sun, J. Power Sources, 2011, **196**, 7763.
24 H.K. Kim, S.M. Bak, K.B. Kim, Electrochem. Commun., 2010, **12**, 1768.
25 H.G. Jung, N. Venugopal, B. Scrosati, Y.K. Sun, J. Power Sources, 2013, **221**, 266.
26 X.J. Yang, D.H. Teng, B.X. Liu, Y.H. Yu, X.P. Yang, Electrochem. Comm., 2011, **13**, 1098-1099.
27 Y. -Q. Wang, L. Gu, Y.-G. Guo, H. Li, X. -Ying He, S. Tsukimoto, Y. Ikuhara and L.-J. Wan, J. Am. Chem. Soc., 2012, **134**, 7874.
28 Y. Liu, X. D. Yan, J.-L. Lan, D.H. Teng, Y.H. Yu, X.P. Yang, 2014, 10.1016/j.electata.2014.05.052 (Unpublished results).
29 D.H. Teng, Y.H. Yu, H.y. Liu, X.P. Yang, S.K. Ryu, Y.H. Lin, Catal. Commun., 2009, **10**, 442.
30 D.H. Teng, Y.H. Yu, X.P. Yang, RSC Adv., 2014, **4**,12309.
31 D.H. Teng, Y.H. Yu, P.W. Li, X. Bai, X.P. Yang, RSC Adv., 2013, **3**, 14237.
32 Z.X. Yang, G.D. Du, Q. Meng, Z.P. Guo, X.B. Yu, Z.X. Chen, T.L. Guo, R. Zeng, J. Mater. Chem., 2012, **22**, 5848.
33 G.D. Du, N. Sharma, V.K. Peterson, J.A. Kimpton, D.Z. Jia, Z.P. Guo, Adv. Funct. Mater., 2011, **21**, 3990.
34 Y. Ma, B. Ding, G. Ji, J.Y. Lee, Nano Lett., 2013, **7**, 10879.

35 T. Xia, W. Zhang, J. Murowchick, G. Liu, X.B. Chen, Nano Lett., 2013, **13,** 5289.
36 K.S. Park, A. Benayad, D. Joon Kang, S.G. Doo, J. Am. Chem. Soc., 2008, **130**, 14930.
37 Peter V. Sushko, Kevin M. Rosso, Ji-Guang Zhang , Jun Liu , and Maria L. Sushko. Adv. Funct. Mater., 2013, **23**, 5530.
38 J.X. Qiu, S. Li, Evan Gray, H.W. Liu, Q.-F. Gu, C.H. Sun, C.Lai, H.J Zhao, S.Q. Zhang. J. Phys. Chem. C, 2014, **118**, 8824.
39 H. Utsunomiya, T. Nakajima, Y. Ohzawa, Z. Mazej, B. Zemva, M. Endo, J. Power Sources, 2010, **195**, 6805.